Article

Fe−Co Bimetallic Catalysts for Pyrolysis of Disposable Face Masks and Nitrile Gloves: Synthesis and Characterization of N-Doped Carbon Nanotubes

He Li, Karen Yuanting Tang, Dingding Yao, Enyi Ye, and Chi-Hwa Wang*

Read Online

ACCESS | Metrics & More | Article Recommendations | SI Supporting Information

ABSTRACT: The global spread of severe acute respiratory syndrome coronavirus 2 has led to a widespread surge in the use of disposable medical face masks (DFMs) and waste nitrile gloves (WNGs). To address the immense disruption in waste management systems, the catalytic pyrolysis of DFMs and WNGs was undertaken to yield multiwalled carbon nanotubes. Two MgO-supported bimetallic catalysts, Fe−Co and Fe−Ni, were synthesized for catalytic pyrolysis. The MgO-supported Fe and Co catalysts showed a good yield of N-doped CNTs (N-CNTs) above 33 wt %, while the percentage of WNGs did not exceed 20 wt %. The pyrolysis process resulted in the formation of Fe−Co microspinels, which were subsequently encapsulated within N-CNTs, ultimately yielding FeCo-NCNTs. The synthesized FeCo-NCNTs were approximately 25 nm in diameter and were extended over several micrometers in length. Subsequent evaluations included testing several acid-washed FeCo-NCNTs as catalysts for the oxygen reduction reaction. The FeCo-NCNTs exhibited remarkable catalytic performance, with a half-wave potential at 0.831 V (vs RHE) and exceptional resistance to methanol poisoning. These remarkable findings have the potential to contribute to the sustainable recycling of waste generated during the COVID-19 pandemic and to the utilization of waste-derived materials.
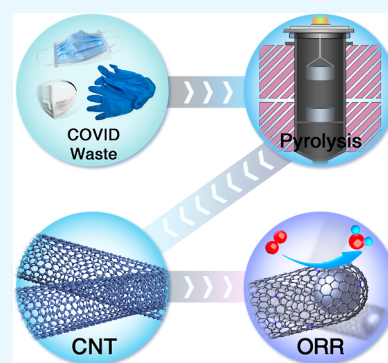
1. INTRODUCTION

Amidst the COVID-19 pandemic, policymakers around the world have implemented measures to mitigate the effects of the virus and protect their population. Public policies including lockdowns and mandatory safe distances have proven effective in controlling the spread of the disease but have also had a negative impact on the economy. In addition, extensive medical testing using polymerase chain reaction and antigen rapid testing has been critical in monitoring and containing the transmission of the virus. However, these public policies and medical testing campaigns have changed the lifestyle of people and led to a significant increase in plastic waste.[1−3] The production of test kits and surgical masks, primarily made from single-use plastics such as polyethylene (PE) and polypropylene (PP), has skyrocketed. Furthermore, implementation of safe distance measures has caused a sharp increase in takeaway services, resulting in a corresponding increase in single-use plastic waste as well. Apart from public policies, the use of personal protective equipment (PPE) in medical settings, including hospitals and clinics, has also surged to protect both healthcare workers and patients. PPE includes surgical caps, surgical/N95 masks, respirators, nitrile gloves, gowns, and goggles, many of which are recommended for single use. While regular change of PPE prevents virus transmission, it also contributes to a significant increase in medical plastic waste.[4,5] While the regular replacement of PPE is critical to preventing the transmission of viruses, it has also contributed to a significant increase in medical plastic waste. Therefore, effective waste management measures are essential to address the environmental concerns arising from increased waste generation during the COVID-19 pandemic.[6−8]

On another front, catalytic pyrolysis has emerged as a promising approach for treatment of a variety of polymer and organic wastes.[9−11] Although recycling is often considered a preferred waste treatment solution, comprehensive research on recycling of various types of plastic waste remains limited.[12,13] In recent years, many researchers have been investigating the conversion of such wastes to value-added materials.[14−16] Pyrolysis, a process that breaks down all types of polymers into smaller molecules, holds great potential in this regard.[17] When these small molecules encounter a suitable catalyst, typically Fe-based, at the right temperature, carbon nanotubes (CNTs) are formed.[18] In particular, the majority of the disposal PPEs is made from plastics such as PP and PE, and considerable research has been conducted to explore their potential as pyrolysis feedstock.[4,19−21] Moreover, medical/laboratory-grade gloves are primarily nitrile gloves made from

nitrile, a synthetic rubber derived from acrylonitrile and butadiene.[22] The existing research on pyrolysis of rubber shows the potential to use medical plastic waste, including nitrile gloves, as a valuable feedstock for CNT production.[23] Additionally, the pyrolysis of used nitrile gloves releases nitrogen, allowing for the production of nitrogen-doped CNTs, expanding the potential applications of this waste-to-resource approach.

Iron-based catalysts have been demonstrated impressive efficiencies in the conversion of waste plastics to CNTs.[24,25] Our earlier research unveiled the potential of Fe−Co or Fe−Ni bimetallic catalysts to achieve high CNTs yield (up to 38.3%) during the pyrolysis of waste plastics.[26] Iron-based catalysts have also demonstrated their versatility as cost-effective alternatives to rare metals in electrocatalysis applications.[2,27,28] For instance, Mn−Fe−Ni oxides nanoparticles have been utilized as trimetallic catalysts for both oxygen reduction reaction (ORR) and oxygen evolution reaction (OER) when supported on multiwalled carbon nanotubes (MWCNTs).[29] Moreover, Fe−Co oxide nanoparticles, when supported on MWCNTs, have exhibited bifunctional OER and ORR activities.[30,31] The similarity in composition and morphology supports the potential of catalytic pyrolysis-derived carbon nanotubes in ORR applications.

In this study, a waste-to-resource pathway was reported that ingeniously recycles disposable medical face masks (DFMs) and waste nitrile gloves (WNGs), common in municipal waste streams, to produce N-CNTs that hold promising potential for electrocatalysis applications. Two different MgO-supported bimetallic catalysts, synthesized by coprecipitation, were used for the pyrolysis of the DFMs and WNGs. Upon evaluation, catalysts with a Fe−Co composition were found to be significantly superior to Fe−Ni in terms of stability and conversion rates, especially as the weight ratio of WNGs in the feedstock increased. Subsequently, the elemental compositions and morphologies of the N-CNTs and Fe−Co particles were investigated. The resulting FeCo-NCNTs were then incorporated into electrode preparations to evaluate their performance in ORR electrocatalysis.

2. METHOD AND MATERIALS

2.1. Materials. DFMs and WNGs were collected as general waste generated in the laboratory and the office at the National University of Singapore without further chemical treatment. All collected wastes were manufactured by local manufacturers licensed by the Singapore Health Sciences Authority. The metal wires in the masks were removed, and DFMs and WNGs were cut into small pieces measuring between 3 and 5 mm. Magnesium chloride hexahydrate ($MgCl_2 \cdot 6H_2O$), iron(III) nitrate nonahydrate [$Fe(NO_3)_3 \cdot 9H_2O$], cobalt(II) nitrate hexahydrate [$Co(NO_3)_2 \cdot 6H_2O$], nickel(II) nitrate hexahydrate [$Ni(NO_3)_2 \cdot 6H_2O$], sodium carbonate (Na_2CO_3), potassium hydroxide (KOH), and 10 wt % platinum on carbon (10% Pt/C) were purchased from Sigma-Aldrich Pte Ltd. All chemicals were used in the experiment without further treatment. Alfa-Aesar carbon paper was purchased from Scientific Resources Pte Ltd. All water used was deionized (18.2 MΩ, Merck Millipore).

2.2. Preparation of Catalysts. The MgO-supported Fe−Co catalysts were prepared as follows: iron(III) nitrate nonahydrate and cobalt(II) nitrate hexahydrate were dissolved in 60 mL of DI water at a molar ratio of 1:1. A certain amount of magnesium chloride hexahydrate was added to the solution

to control the weight ratio of Fe and Co in the final oxides, which was 5 wt % each. Sodium carbonate solution was added dropwise to the solution to gradually increase the pH. The precipitate was collected when the pH reached 8. The as-collected precipitate was washed with DI water and dried at 150 °C overnight. Subsequently, the precipitate was transferred into a furnace to be activated at 800 °C for 3 h and then used as a catalyst in pyrolysis. The MgO-supported Fe−Ni catalyst was prepared by the same method.

2.3. Experiment of Catalytic Pyrolysis. The experiment was performed in a fixed-bed tube reactor, which was divided into two stages, as shown in Figure S1. In the upper stage, a quartz boat was suspended to place the feedstock for pyrolysis. The quartz boat in the lower section was placed on a platform. Both boats had holes in the bottom to allow gas flow to pass through. The feedstock was prepared by placing small pieces of mask and nitrile, with the weight of each material estimated to prepare feedstock with different weight ratios. In the lower boat, 0.4 g of catalyst was placed to capture and deposit CNTs. The temperature program first increased the temperature of the lower section to 800 °C and then started heating the upper section to 500 °C at 15 °C min^{-1}. The reaction time was 50 min after the lower section reached 800 °C. The optimum reaction temperature was tested in our previous experiments.[32] The gas products were collected in gas sampling bags and later sent for gas analysis. The weight of the bottom boat was measured, and the change in weight after the reaction was calculated. The yield of carbon nanotubes was measured based on the increase in weight of the lower boat after the pyrolysis. The pyrolysis was performed under a N_2 atmosphere at a flow rate of 100 mL min^{-1}.

2.4. Analysis and Characterizations. A field emission scanning electron microscope (JSM-6700F) was implemented to reveal the morphology of samples. A high-resolution field emission transmission electron microscope (JEM-2100F) was applied to investigate the structures of samples. The CNT samples were first dispersed in ethanol with the help of ultrasonication. The suspension was dropped onto a carbon-coated copper mesh grid. X-ray photoelectron spectroscopy (XPS, AXIS-HSi, Kratos Analytical) was conducted to measure the elemental composition of the samples. The gas effluent was collected by using a gas sampling bag and sent to gas chromatography (GC, PerkinElmer, Clarus 580) for gas composition analysis. The liquid samples were analyzed by mass spectrometry coupled to gas chromatography (GC−MS, Agilent 5975). The electrochemical performance was analyzed by using an electrochemical workstation (AUTOLAB PGSTAT302N). Thermogravimetric analysis (TGA) was performed in air from room temperature to 800 °C at 20 °C min^{-1}

2.5. Electrochemistry Analysis. Different carbon nanotube samples were ground for 30 min prior to ORR electrochemical analysis. Each sample was mixed with Nafion solution at a CNTs-to-Nafion ratio of 9:1 and dissolved in a 1:1 mixture of water and ethanol to prepare the catalyst ink. All mixtures were sonicated for 30 min to ensure that the samples were well-dispersed. A three-electrode cell was prepared in a typical manner using a Hg/HgO electrode with 0.1 M KOH solution as the reference electrode and a graphite electrode as the counter electrode instead of platinum to avoid the accumulation of platinum on the electrode surfaces. For each test, 10 μL of catalyst ink was drop-cast onto a rotating disk electrode (RDE, PINE Research, 5 mm in diameter) and

allowed to dry at room temperature. RDE cyclic voltammetry (CV) was performed in an N_2-saturated 0.1 M KOH solution to activate the catalysts. RDE linear sweep voltammetry (LSV) was performed in an O_2-saturated solution. The potential was calibrated from vs Hg/HgO to vs RHE (reversible hydrogen electrode) using the following equation

$$E(\text{vs RHE}) = E_{\text{Hg/HgO}} + 0.059 \times \text{pH} + E^{\circ}_{\text{Hg/HgO}} \qquad (1)$$

where $E^{\circ}_{\text{Hg/HgO}}$ is the standard potential of the Hg/HgO electrode.

3. RESULTS AND DISCUSSION

3.1. Catalytic Pyrolysis. The SEM images in Figure 1 present the morphologies of the synthesized Fe−Co and Fe−
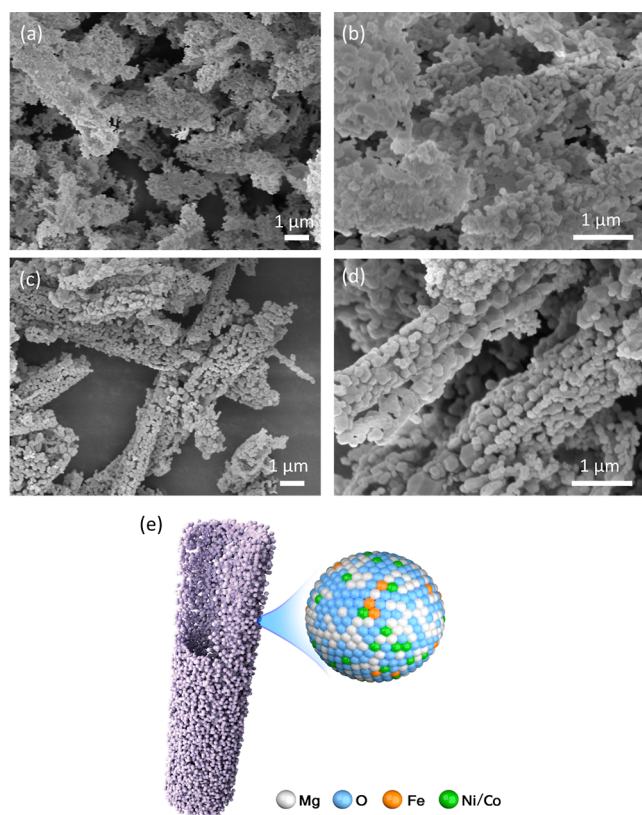

Figure 1. FE-SEM images of catalysts before and after pyrolysis: (a,b) Fe−Co catalyst and (c,d) Fe−Ni catalyst. (e) 3D illustration of fresh catalysts prepared by the coprecipitation method.

Ni catalysts. Evidently, the formation of aggregated "coblike" structures from the metal oxide nanoparticles is common to both catalysts (Figure 1e). The distinct morphology of these catalysts, when compared to that of MgO powder, strongly suggests the synthesis of spinels such as ferrite spinels. It helps the uniform distribution of Fe and Co in the catalysts and formation of Fe−Co microspinels. Previous research indicates that such microspinels can significantly facilitate the synthesis of carbon nanotubes and increase the downstream H_2 yield.[32] The elemental analysis, as shown in Table S1, indicates that each of the elements Fe, Co, and Ni have a loading of approximately 4.5 wt %. The elemental analysis of the feedstock (WNGs and DFMs) is shown in Table S2. WNGs exhibit a nitrogen content of 8.51% by weight, which corresponds to a mole ratio of carbon to nitrogen of

approximately 10:1. The nonwoven fabric within the DFMs appears to be composed of PP or PE based on elemental analysis, with a carbon to hydrogen atomic ratio of approximately 0.5 (mass ratio of 6.1). Meanwhile, the TGA profiles further reveal that WNGs lose about 80% of their weight at 500 °C (Figure S2), whereas DFMs undergo almost complete weight loss at the same temperature (Figure S3). Mass spectrometry results suggest the release of small molecules from both materials at temperatures above 400 °C.

During the catalytic pyrolysis, the temperature of the lower stage was first escalated to 800 °C to activate the catalyst. The upper stage temperature was then increased to 500 °C to facilitate decomposition of the feedstock. The feedstock consisted of a mixture of WNGs and DFMs with different weight ratios, and the yields of different products from the different compositions of the mixture are summarized in Table 1.

Table 1. Gas and Carbon Productions from Different Feedstocks with Different Catalysts

catalysts	Fe−Co catalyst				Fe−Ni catalyst	
WNGs weight percentage	0%	10%	20%	30%	0%	10%
gas yield, wt %	41.59	40.37	39.79	38.75	42.63	37.11
liquid yield, wt %	24.22	25.55	26.43	51.34	23.16	52.16
carbon yield, wt %	34.19	34.08	33.78	9.91	34.21	10.73
Gas Composition						
H_2	42.03	43.99	40.64	23.12	44.05	22.71
CH_4	37.99	37.95	37.85	34.01	37.46	33.81
CO	3.87	3.38	4.14	2.98	2.90	3.92
CO_2	1.19	1.57	1.29	1.49	1.25	1.37
C_{2+}	14.92	13.11	16.08	38.40	14.34	38.19

The yields of carbon nanotubes (CNTs) obtained from different feedstocks and catalysts manifest different chemical affinities of the two catalysts toward active nitrogen. When 100% DFMs are employed as the feedstock, the CNT yield peaks at 34.2% with both catalysts. However, the Fe−Ni catalyst outperforms Fe−Co in terms of the yields of CNTs, H_2, and CH_4. Nevertheless, as the weight percentage of WNGs in the mixture increases to 10%, the yield of CNTs decreases to 10.7% by using the Fe−Ni catalyst. Remarkably, even when the weight percentage of the WNGs escalates to 20%, the yield of CNTs remains relatively stable at 33.8%. When the weight percentage of WNGs increases to 30%, there is a noticeable decline in the carbon yield to 9.9% and a dramatic increase in the liquid yield to 51.34%. This decrease in conversion can be attributed to the overproduction of nitrogen or ammonia from WNG decomposition. The pyrolysis results of DFMs are consistent with those obtained from the catalytic pyrolysis of PE or PP using the same catalyst, confirming the validity of the elemental analysis. This suggests that DFMs can be processed like many other types of plastic waste. Furthermore, WNGs are composed of nitrile-butadiene rubber (NBR), a synthetic rubber that is a copolymer of acrylonitrile and butadiene.[33] The degradation of NBR results in the formation of nitrogen-containing molecules and radicals. A possible explanation for the decreasing CNT yield with an increasing WNGs ratio is the potential coordination of metal ions in the catalysts with one or more nitrogen atoms, which may subsequently interfere with the pyrolysis reaction.

The GC−MS analysis of the liquid products (Table 2) reveals that a majority of the products collected from the

Table 2. Composition Analysis of the Pyrolytic Oil

component	feedstock (area %)	
	100% DFMs	80% DFMs + 20% WNGs
phenanthrene	46.57	43.76
naphthalene	5.53	6.12
2-phenyl-naphthalene	5.68	4.89
2-ethenyl-naphthalene	4.56	5.31
chrysene	4.15	4.76
2,2′-binaphthalene	3.65	2.91
fluorene	2.27	3.09
1-phenyl-naphthalene	2.09	1.90
1-phenylindene	1.76	1.72
fluoranthene	1.66	1.68
(Z)-9-tricosene	1.70	1.72
methyl-anthracene	1.51	1.67
diphenyl-1,3-butadiyne	1.29	2.53
other polycyclic aromatic hydrocarbons[a]	17.58	17.94

[a]Compositions lower than 1.5 wt % each in both samples.

condensers are polycyclic aromatic hydrocarbons (PAHs). The relative content of phenanthrene, a PAH, exceeds 40%, which is consistent with the composition of tar derived from pyrolysis of biomass materials.[34] Given that the feedstock materials do not contain any aromatic hydrocarbons, this confirms the ability of the Fe−Co−Mg catalyst to synthesize phenyl groups or aromatic rings. Incorporation of WNGs does not notably alter the composition of the pyrolytic oil, indicating that the formation of PAHs is relatively independent of the feedstock composition and the presence of nitrogen. The amount of each naphthalene derivative in the pyrolysis products of both samples is lower than that of naphthalene itself, which can be attributed to their rapid consumption in the formation of solid products such as soot or nanotubes.[35]

3.2. Characterization. Figure 2a,b illustrates the entanglement of synthesized graphitic CNTs with catalyst particles when the feedstock consists of 20% WNGs. As the percentage
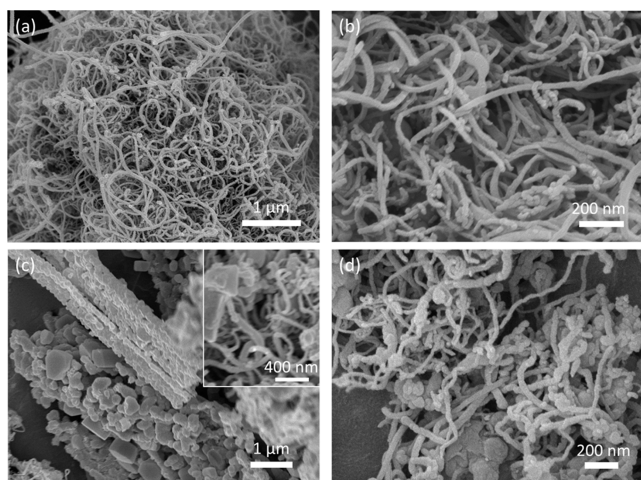
Figure 2. FE-SEM images of catalysts after pyrolysis: (a,b) FeCo-NCNT-p when weight percentage of WNGs is 20%. (c,d) Fe−Co after reaction with 30% WNGs in feedstock.

of WNGs increases to 30%, the SEM images show that some parts of the Fe−Co catalyst are enveloped by carbon (Figure 2c). At this stage, only amorphous structures or short nanotubes are visible (Figure 2d). While the presence of nitrogen could potentially hinder the growth of CNTs, it offers a new way to prepare N-doped CNTs from waste polymers. Therefore, two different samples were prepared for further characterization. The carbon nanotube synthesized from 100% DFMs is categorized as pristine CNTs (abbreviated as FeCo-CNT-p), while the one synthesized from the mixture containing 20% WNGs is categorized as N-doped CNTs (abbreviated as FeCo-NCNT-p). Both samples were washed with dilute hydrochloric acid before further characterization. The acid-washed CNT and N-CNT samples were labeled as FeCo-CNT and FeCo-NCNT, respectively.

The TEM images of FeCo-CNTs and FeCo-NCNTs are presented in Figure 3. The diameter and length of FeCo-CNTs
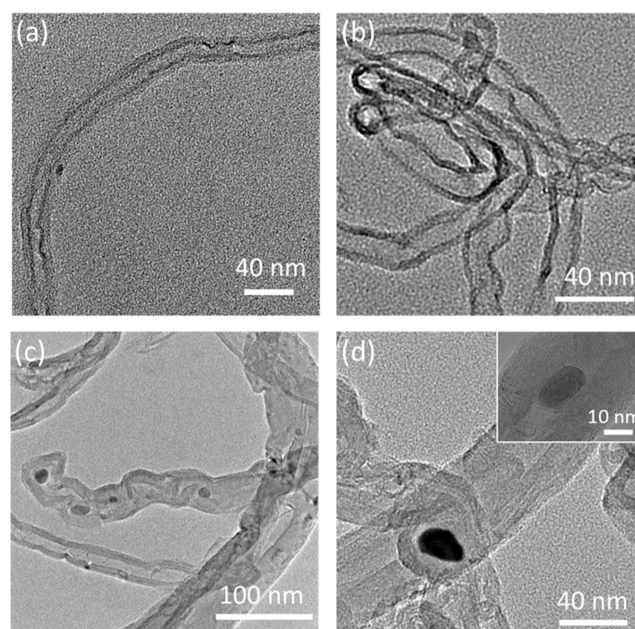
Figure 3. FE-TEM images of a carbon nanotube from the Fe−Co catalyst after pyrolysis: (a) FeCo-CNT-p, (b) FeCo-NCNT-p, (c) Fe−Co nanoparticles encapsulated in FeCo-CNT-p. (d) Fe−Co nanoparticles encapsulated in FeCo-NCNT-p.

(Figure 3a) and FeCo-NCNTs (Figure 3b) did not show significant variations. These waste-derived CNTs are MWCNTs, and their lengths range from hundreds of nanometers to tens of micrometers, with an outer diameter of about 30 nm. Figure 3c,d shows nanoparticles encapsulated at the end of the nanotubes, most of which measure around 10 nm in diameter. Meanwhile, the SEM-EDS results (Figure S4) identify some metallic nanoparticles that are not completely encapsulated by CNTs.

The XRD patterns shown in Figure 4a,b reveal the contrast before and after the pyrolysis of both Fe−Ni and Fe−Co catalysts. The dominant peaks in the XRD patterns are attributed to MgO, but the significant peaks of Fe_2O_3, NiO, and CoO overlap with these. The appearance of a peak of $Mg_{1.6}Fe_{1.6}O_4$ in the XRD of both fresh catalysts, which disappears in the FeCo-CNT samples, suggests that oxides other than MgO are reduced during the reaction. In addition, the peaks at 26 and 43° in both FeCo-CNT-p and FeCo-
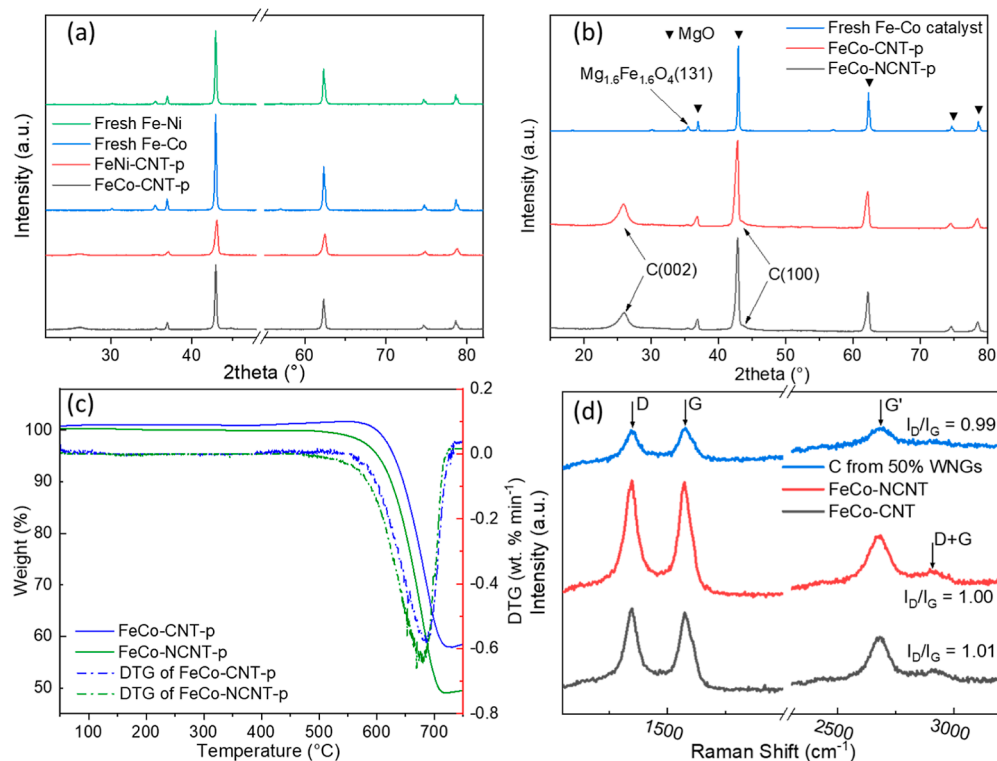
Figure 4. (a) XRD patterns of Fe−Ni and Fe−Co catalysts before and after pyrolysis reaction. (b) XRD patterns of three different Fe−Co catalyst samples before and after pyrolysis. (c) Thermogravimetric analysis of FeCo-NCNT-p. (d) Raman spectra of different carbon samples.
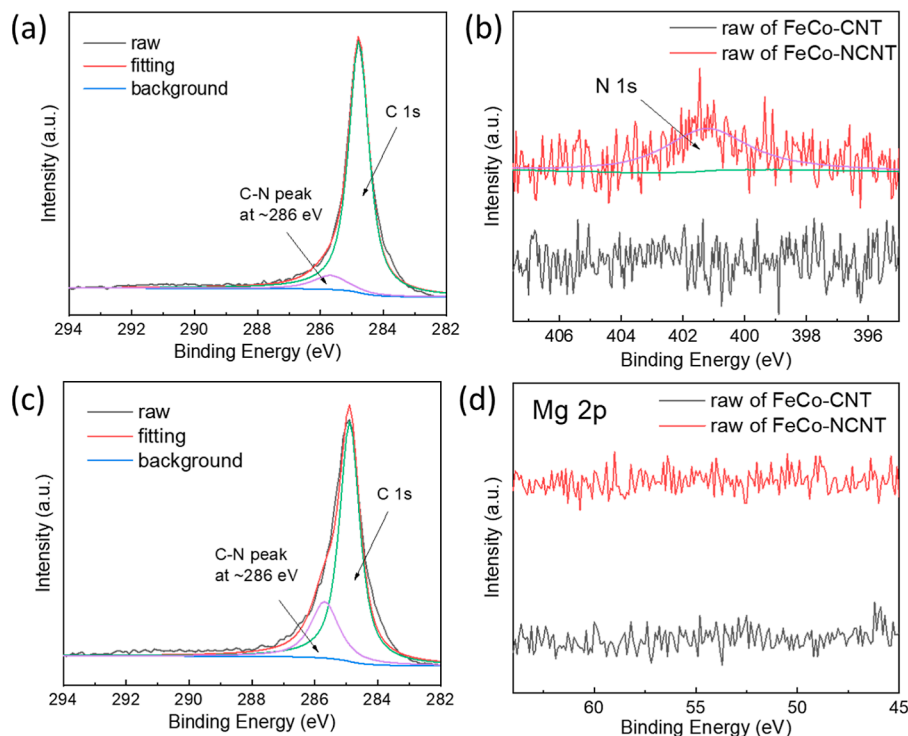

Figure 5. XPS spectra of (a) C 1s peak of FeCo-CNTs, (b) N 1s peaks of both FeCo-CNTs and FeCo-NCNTs, (c) C 1s peak of N-CNTs, and (d) Mg 2p peaks of FeCo-CNTs and FeCo-NCNTs.

NCNT-p suggest the presence of graphitic carbon. The formation of $Mg_{1.6}Fe_{1.6}O_4$ suggests that coprecipitation helps other metal ions uniformly distributed in the catalyst support (MgO) and MgO remains unchanged after pyrolysis reactions, while Fe was reduced as the peak of $Mg_{1.6}Fe_{1.6}O_4$ vanished

after the reaction. The XPS patterns reveal the oxidation states of Co and Ni and their oxygen in Fe−Co and Fe−Ni, respectively (Figure S5).

The TGA and differential thermal analysis profiles in Figure 4c show that both samples have only one major peak at 670
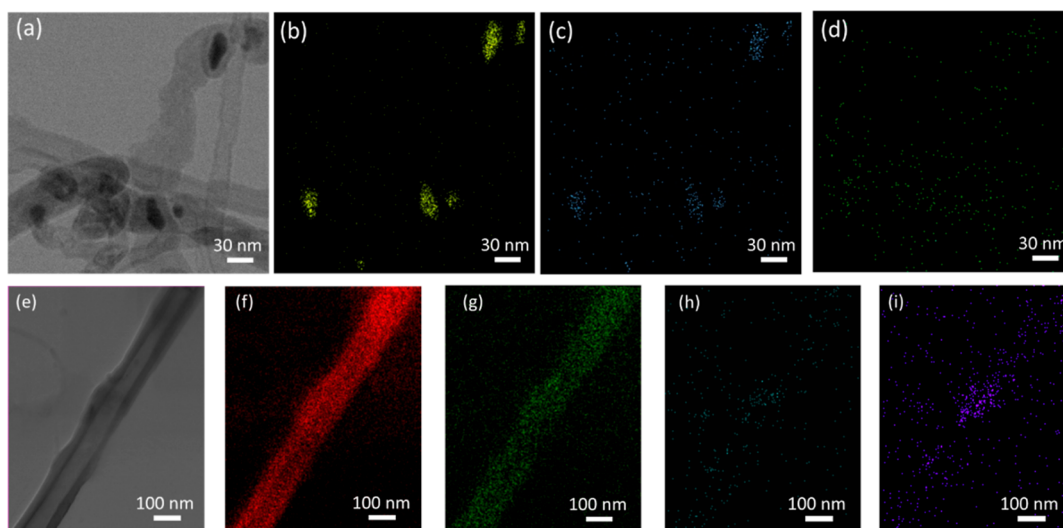
Figure 6. TEM image of FeCo-NCNTs (a) and corresponding elemental mappings of (b) iron, (c) cobalt, and (d) magnesium. TEM images of single FeCo-CNT (e) and elemental mapping of (f) carbon, (g) nitrogen, (h) cobalt, and (i) iron.

°C, and their weight loss before 500 °C is less than 1%. This indicates that the composition of carbon black and pyrolytic carbon is negligible. Comparing the peak of FeCo-NCNT, the peak of FeCo-CNT appears at a higher temperature, implying thicker tube walls and fewer defects. In Figure 4d, the Raman spectra of three different carbon samples are similar. Although the Raman intensity depends on the yield of carbon nanotubes on catalysts, the D-band, G-band, and G'-band of the three samples remain comparable. The incorporation of nitrogen atoms does not significantly affect the morphology and crystallinity of the samples as the ratio of the D-band and G-band intensity is approximately 1 for three different samples.

XPS was used to further investigate the chemical composition and state of the samples (FeCo-CNTs and FeCo-NCNTs). While carbon appears as a robust single peak in both XPS patterns, a difference is observed between these two samples. Compared to the C peaks of FeCo-CNTs (Figure 5a), the C peak of FeCo-NCNTs is right-skewed (Figure 5c), indicating an overlapping peak at about 286 eV. The main peak of C 1s located at 284.8 eV represents the binding energy of carbon in the C−C bond, while the peaks located slightly higher than 285 eV indicate the carbon atoms bonded to oxygen and nitrogen with a single bond.[36,37] Moreover, the high-resolution spectra of nitrogen confirm that NBR from WNGs has been successfully used as a nitrogen source, introducing nitrogen into the carbon products. The N 1s pattern shows a broad peak centered at 401.8 eV. This binding energy is close to that of pyrrole at 400.7 eV of pyrrole and alkylammonium at 402.4 eV but higher than the binding energy of nitrile 399.4 eV.[38] Interestingly, Fe, Co, and Mg were not detected in either sample (Figure S6). The XPS spectra show only noise, suggesting that most of the unencapsulated metal component was thoroughly removed after the acid wash. Given that the typical depth of XPS analysis is around 5 nm, it is reasonable that the encapsulated nanoparticles are not detected by XPS. This could also explain the weak signal of the N 1s peak. The elemental analysis of FeCo-NCNTs in Table S3 proves that the acid wash did not completely remove the metallic component and that about 60% of nitrogen was deposited in the N-CNTs.

The TEM−EDS results provide several insights into the chemical composition. In Figure 6, the elemental mapping signal of Fe and Co aligns strongly with the positions of the encapsulated nanoparticles, suggesting that the encapsulated nanoparticles are Fe−Co microspinels situated inside the tube. Notably, although the Fe−Co−Mg catalyst was prepared by the coprecipitation method, the distribution of Fe and Co is significantly different from that of Mg. As a catalyst support, Mg or MgO was not encapsulated with Fe and Co since the elemental mapping of FeCo-NCNTs did not show a strong signal of Mg. This suggests that MgO was not involved in the growth of the CNTs. Moreover, this indicates that the encapsulated Fe−Co nanoparticles are resistant to acidic solutions.

TEM images of a single nanotube were taken to facilitate a detailed examination of the N-CNTs. Figure 6e displays a TEM image of a single nanotube from the FeCo-NCNTs, along with the corresponding TEM−EDX elemental mapping results. The as-synthesized CNTs are MWCNTs with diameters in the range of 20−30 nm. The C mapping and N mapping in Figure 6f,g correlate strongly with the location of the carbon nanotube in Figure 6e. However, the nitrogen mapping is relatively weaker than the mapping of C due to its low concentration. In contrast, the correlation between the location of the nanotube and the intense mapping of Co and Fe is less pronounced. This suggests that the Co and Fe atoms do not intercalate in the growth of the carbon nanotubes, implying that these metal atoms do not significantly influence the formation and structure of the nanotubes. This result provides valuable information for understanding the synthesis of N-CNTs and the role of catalysts in their formation.

3.3. Oxygen Reduction Reaction. The catalyst consisting of Fe−Co nanoparticles is first activated in an N_2-saturated KOH solution by CV, as shown in Figure S7. These Fe−Co nanoparticles are considered to be the active site in these catalysts, as demonstrated in Figure 7a. The LSV curves of different samples were compared using a 10 wt % Pt/C catalyst as a reference (Figure 7b). The FeCo-NCNTs exhibited a high half-wave potential of 0.831 V, which is 31 mV lower than that of the 10% Pt/C catalyst, as well as a high positive onset potential of 0.925 V (where the current density is 0.1 mA
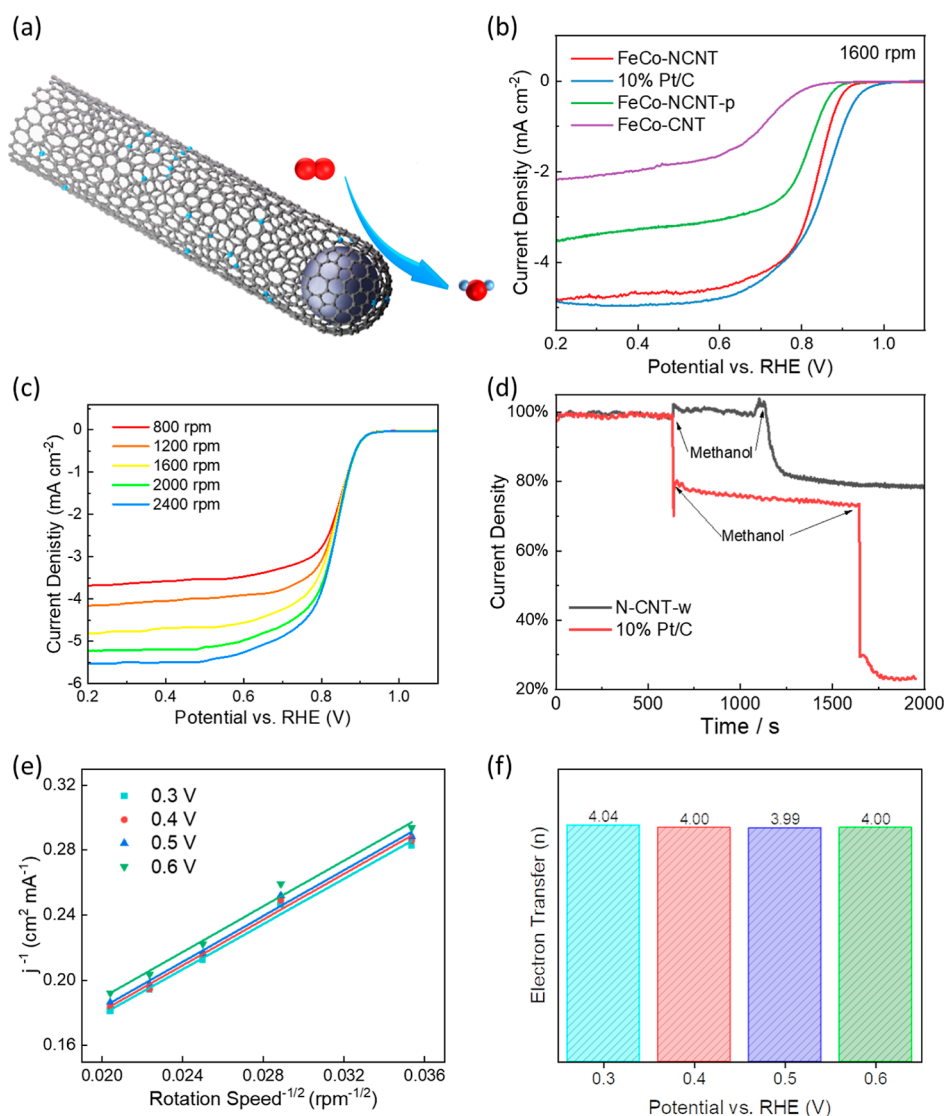
Figure 7. (a) Illustration of the ORR on FeCo-NCNTs. (b) LSV result of different samples from 0.2 to 1.1 V vs RHE. (c) LSV curves of FeCo-NCNTs under different RDE rotation speeds. (d) Chronoamperometric responses of FeCo-NCNTs and 10% Pt/C at 0.6 V in an O_2-saturated 0.1 M KOH solution. (e) Koutecky−Levich plot of the ORR at different electrode potentials on FeCo-NCNTs. (f) Estimated numbers of electron transferred at different electrode potentials.

cm^{-2}). Compared with 10% Pt/C, FeCo-NCNTs exhibited significantly higher resistance to methanol. In Figure 7d, when the methanol concentration was increased to 2% and then to 4% in the KOH electrolyte, the current of the FeCo-NCNTs was maintained at 100% for 2 vol % methanol and 79% for 4 vol % methanol. In comparison, the current of the 10% Pt/C catalyst decreased to 71% after the addition of 2% methanol and decreased to 20% of its initial value when the methanol concentration reached 4% by volume. The kinetics of the ORR were investigated by measuring the electrochemical behavior of the FeCo-NCNTs at different rotation speeds of the RDE, as shown in Figure 7c. The linear fitting lines were calculated and are plotted in Figure 7e. As the rotation speed increased, the mass transfer near the electrode was improved, resulting in a faster oxygen diffusion around the active sites. This Koutecky−Levich plot suggested first-order reaction kinetics and helps to estimate the number of electrons transferred during the ORR. The linear fitting results of the K-L plot indicate that the numbers of electrons transferred are 4.00, 3.99, and 4.00 at 0.4, 0.5, and 0.6 V, respectively (Figure 7f).

4. CONCLUSIONS

This study presents a waste-to-resource pathway that effectively recycles DFMs and WNGs generated in large quantities during the COVID-19 pandemic. The developed synthetic route not only enables the production of N-CNTs, but also provides an approach for the treatment of these two highly prevalent wastes. Through catalytic pyrolysis, the Fe−Co catalyst demonstrated its efficacy in the conversion of the waste materials into N-doped CNTs, achieving a CNT yield of over 30% when the WNGs content in the feedstock were not greater than 20% by weight. Conversely, the Fe−Ni catalyst was found to be susceptible to poisoning when the WNGs content reached 10 wt %.

In addition, the waste-derived FeCo-NCNTs exhibited desirable electrocatalytic properties, with a comparable half-wave potential of 831 mV and exceptional resistance to methanol during the ORR. The results of this study highlight the importance of innovative approaches for converting waste into valuable resources. Catalytic pyrolysis provides a means to

obtain N-CNTs with promising electrocatalytic properties, while at the same time reducing the environmental impact of pandemic-generated waste. These advances provide insights into addressing pandemic pollution challenges and contribute to sustainable waste management solutions. Further research can explore the broader application potential of waste-derived materials, promoting a circular economy and sustainable practices.

ASSOCIATED CONTENT

Ⓢ Supporting Information

The Supporting Information is available free of charge at https://pubs.acs.org/doi/10.1021/acsomega.3c05708.

> Scheme diagram of a catalytic pyrolysis furnace; TGA and MS curves of WNGs and DFMs in N_2; metal composition analysis of fresh catalysts; CHNS analysis of WNGs and DFMs; SEM images of FeCo-CNT-p and elemental mapping; XPS spectra of the Fe−Co catalyst, Fe−Ni catalyst, and FeCo-NCNT; element analysis of N-doped CNT from catalytic pyrolysis; and CV curve of FeCo-NCNT in N_2-saturated solution (PDF)

AUTHOR INFORMATION

Corresponding Author

Chi-Hwa Wang − *Department of Chemical and Biomolecular Engineering, National University of Singapore, Singapore 117585, Singapore;* Ⓞ orcid.org/0000-0002-1040-2121; Phone: +65-65165079; Email: chewch@nus.edu.sg

Authors

He Li − *NUS Environmental Research Institute (NERI), National University of Singapore, Singapore 138602, Singapore; Energy and Environmental Sustainability Solutions for Megacities (E2S2), Campus for Research Excellence and Technological Enterprise (CREATE), Singapore 138602, Singapore; Department of Chemical and Biomolecular Engineering, National University of Singapore, Singapore 117585, Singapore*

Karen Yuanting Tang − *Department of Chemical and Biomolecular Engineering, National University of Singapore, Singapore 117585, Singapore; Institute of Materials Research and Engineering, Agency for Science, Technology, and Research (A*STAR), Singapore 138634, Singapore*

Dingding Yao − *NUS Environmental Research Institute (NERI), National University of Singapore, Singapore 138602, Singapore; School of Engineering, Huazhong Agriculture University, Wuhan 430000, China*

Enyi Ye − *Institute of Materials Research and Engineering, Agency for Science, Technology, and Research (A*STAR), Singapore 138634, Singapore;* Ⓞ orcid.org/0000-0002-2398-0676

Complete contact information is available at:
https://pubs.acs.org/10.1021/acsomega.3c05708

Notes

The authors declare no competing financial interest.

ACKNOWLEDGMENTS

REFERENCES

(1) Górnicka, M.; Drywień, M. E.; Zielinska, M. A.; Hamułka, J. Dietary and lifestyle changes during COVID-19 and the subsequent lockdowns among Polish adults: a cross-sectional online survey PLifeCOVID-19 study. *Nutrients* **2020**, *12* (8), 2324.

(2) Chakraborty, B.; Beltrán-Suito, R.; Hausmann, J. N.; Garai, S.; Driess, M.; Menezes, P. W. Enabling iron-based highly effective electrochemical water-splitting and selective oxygenation of organic substrates through in situ surface modification of intermetallic iron stannide precatalyst. *Adv. Energy Mater.* **2020**, *10* (30), 2001377.

(3) Cancello, R.; Soranna, D.; Zambra, G.; Zambon, A.; Invitti, C. Determinants of the lifestyle changes during COVID-19 pandemic in the residents of Northern Italy. *Int. J. Environ. Res. Public Health* **2020**, *17* (17), 6287.

(4) Sharma, H. B.; Vanapalli, K. R.; Cheela, V. S.; Ranjan, V. P.; Jaglan, A. K.; Dubey, B.; Goel, S.; Bhattacharya, J. Challenges, opportunities, and innovations for effective solid waste management during and post COVID-19 pandemic. *Resour., Conserv. Recycl.* **2020**, *162*, 105052.

(5) Patrício Silva, A. L.; Prata, J. C.; Walker, T. R.; Duarte, A. C.; Ouyang, W.; Barcelò, D.; Rocha-Santos, T. J. C. E. J. Increased plastic pollution due to COVID-19 pandemic: Challenges and recommendations. *Chem. Eng. J.* **2021**, *405*, 126683.

(6) Hossain, R.; Islam, M. T.; Ghose, A.; Sahajwalla, V. Full circle: Challenges and prospects for plastic waste management in Australia to achieve circular economy. *J. Cleaner Prod.* **2022**, *368*, 133127.

(7) Liu, M.; Wen, J.; Feng, Y.; Zhang, L.; Wu, J.; Wang, J.; Yang, X. A benefit evaluation for recycling medical plastic waste in China based on material flow analysis and life cycle assessment. *J. Cleaner Prod.* **2022**, *368*, 133033.

(8) Galanakis, C. M.; Brunori, G.; Chiaramonti, D.; Matthews, R.; Panoutsou, C.; Fritsche, U. R. Bioeconomy and green recovery in a post-COVID-19 era. *Sci. Total Environ.* **2022**, *808*, 152180.

(9) Lee, D. J.; Jeong, K. H.; Lee, D. H.; Lee, S. H.; Jung, M. W.; Jang, Y. N.; Jo, G. G.; Kwag, J. H.; Yi, H.; Park, Y. K.; et al. Catalytic pyrolysis of swine manure using CO_2 and steel slag. *Environ. Int.* **2019**, *133* (Pt B), 105204.

(10) Wan Mahari, W. A.; Kee, S. H.; Foong, S. Y.; Amelia, T. S. M.; Bhubalan, K.; Man, M.; Yang, Y.; Ong, H. C.; Vithanage, M.; Lam, S. S.; et al. Generating alternative fuel and bioplastics from medical plastic waste and waste frying oil using microwave co-pyrolysis combined with microbial fermentation. *Renewable Sustainable Energy Rev.* **2022**, *153*, 111790.

(11) Nishu; Li, C.; Yellezuome, D.; Li, Y.; Liu, R. Catalytic pyrolysis of rice straw for high yield of aromatics over modified ZSM-5 catalysts and its kinetics. *Renewable Energy* **2023**, *209*, 569−580.

(12) Liang, Y. Y.; Tan, Q. Y.; Song, Q. B.; Li, J. H. An analysis of the plastic waste trade and management in Asia. *Waste Manage. Res.* **2021**, *119*, 242−253.

(13) Faraca, G.; Astrup, T. Plastic waste from recycling centres: Characterisation and evaluation of plastic recyclability. *Waste Manage. Res.* **2019**, *95*, 388−398.

(14) Han, Y.; Yu, J.; Chen, T.; Liu, X.; Sun, L. Study on catalytic pyrolysis mechanism of natural rubber (NR) over Zn-modified ZSM5 catalysts. *J. Energy Inst.* **2021**, *94*, 210−221.

(15) Li, Q.; Faramarzi, A.; Zhang, S.; Wang, Y.; Hu, X.; Gholizadeh, M. Progress in catalytic pyrolysis of municipal solid waste. *Energy Convers. Manage.* **2020**, *226*, 113525.

(16) Cai, N.; Xia, S. W.; Li, X. Q.; Xiao, H. Y.; Chen, X.; Chen, Y. Q.; Bartocci, P.; Chen, H. P.; Williams, P. T.; Yang, H. P. High-value products from ex-situ catalytic pyrolysis of polypropylene waste using iron-based catalysts: the influence of support materials. *Waste Manage. Res.* **2021**, *136*, 47−56.

(17) Martínez-Narro, G.; Prasertcharoensuk, P.; Diaz-Silvarrey, L. S.; Dixon, L.; Phan, A. N. Chemical recycling of mixed plastic waste via catalytic pyrolysis. *J. Environ. Chem. Eng.* **2022**, *10* (5), 108494.

(18) Hernadi, K.; Fonseca, A.; Nagy, J. B.; Bernaerts, D.; Lucas, A. A. Fe-catalyzed carbon nanotube formation. *Carbon* **1996**, *34* (10), 1249−1257.

(19) Chen, N.; Koker, M. K.; Uzun, S.; Silberstein, M. N. In-situ X-ray study of the deformation mechanisms of non-woven polypropylene. *Int. J. Solids Struct.* **2016**, *97-98*, 200−208.

(20) Zhu, Y.; Miao, J.; Long, M.; Wu, C. Feasibilities of producing high-value carbon nanotubes from waste plastics by spray pyrolysis. *J. Anal. Appl. Pyrolysis* **2022**, *166*, 105613.

(21) Zhu, Y.; Miao, J.; Zhang, Y.; Li, C.; Wang, Y.; Cheng, Y.; Long, M.; Wang, J.; Wu, C. Carbon nanotubes production from real-world waste plastics and the pyrolysis behaviour. *Waste Manage. Res.* **2023**, *166*, 141−151.

(22) Coran, A.; Patel, R. Rubber-thermoplastic compositions. Part VIII. Nitrile rubber polyolefin blends with technological compatibilization. *Rubber Chem. Technol.* **1983**, *56* (5), 1045−1060.

(23) Yu, J.; Liu, S.; Cardoso, A.; Han, Y.; Bikane, K.; Sun, L. Catalytic pyrolysis of rubbers and vulcanized rubbers using modified zeolites and mesoporous catalysts with Zn and Cu. *Energy* **2019**, *188*, 116117.

(24) Williams, P. T. Hydrogen and carbon nanotubes from pyrolysis-catalysis of waste plastics: A review. *Waste Biomass Valorization* **2021**, *12* (1), 1−28.

(25) Liu, M.; Yan, X.; Su, L.; Dong, H.; Hu, Z.; Peng, Y.; Guan, L.; Zhang, J.; Zhou, Z.; Zhu, Y.; et al. Waste plastic thermal-transformed CNT@Fe−Mo/MgO for free radical activation and bacteria sterilization. *J. Cleaner Prod.* **2022**, *373*, 133794.

(26) Yao, D.; Li, H.; Mohan, B. C.; Prabhakar, A. K.; Dai, Y.; Wang, C.-H. Conversion of waste plastic packings to carbon nanomaterials: investigation into catalyst material, waste type, and product applications. *ACS Sustain. Chem. Eng.* **2022**, *10* (3), 1125−1136.

(27) Yu, M.; Budiyanto, E.; Tuysuz, H. Principles of water electrolysis and recent progress in cobalt-, nickel-, and iron-based oxides for the oxygen evolution reaction. *Angew. Chem., Int. Ed.* **2022**, *61* (1), No. e202103824.

(28) Park, J. W.; Park, G.; Kim, M.; Han, M.; Jang, J.; Yamauchi, Y.; Yuliarto, B.; Krüger, P.; Kim, J.; Park, N.; et al. Ni-single atom decorated mesoporous carbon electrocatalysts for hydrogen evolution reaction. *Chem. Eng. J.* **2023**, *468*, 143733.

(29) Morales, D. M.; Kazakova, M. A.; Dieckhöfer, S.; Selyutin, A. G.; Golubtsov, G. V.; Schuhmann, W.; Masa, J. Trimetallic Mn-Fe-Ni oxide nanoparticles supported on multi-walled carbon nanotubes as high-performance bifunctional ORR/OER electrocatalyst in alkaline media. *Adv. Funct. Mater.* **2020**, *30* (6), 1905992.

(30) Elumeeva, K.; Kazakova, M. A.; Morales, D. M.; Medina, D.; Selyutin, A.; Golubtsov, G.; Ivanov, Y.; Kuznetzov, V.; Chuvilin, A.; Antoni, H.; et al. Bifunctional oxygen reduction/oxygen evolution activity of mixed Fe/Co oxide nanoparticles with variable Fe/Co ratios supported on multiwalled carbon nanotubes. *ChemSusChem* **2018**, *11* (7), 1204−1214.

(31) Kim, M.; Firestein, K. L.; Fernando, J. F. S.; Xu, X.; Lim, H.; Golberg, D. V.; Na, J.; Kim, J.; Nara, H.; Tang, J.; et al. Strategic design of Fe and N co-doped hierarchically porous carbon as superior ORR catalyst: from the perspective of nanoarchitectonics. *Chem. Sci.* **2022**, *13* (36), 10836−10845.

(32) Yao, D.; Li, H.; Dai, Y.; Wang, C.-H. Impact of temperature on the activity of Fe-Ni catalysts for pyrolysis and decomposition processing of plastic waste. *Chem. Eng. J.* **2021**, *408*, 127268.

(33) Rego, A.; Roley, L. In-use barrier integrity of gloves: Latex and nitrile superior to vinyl. *Am. J. Infect. Control* **1999**, *27* (5), 405−410.

(34) McGrath, T.; Sharma, R.; Hajaligol, M. An experimental investigation into the formation of polycyclic-aromatic hydrocarbons (PAH) from pyrolysis of biomass materials. *Fuel* **2001**, *80* (12), 1787−1797.

(35) Shukla, B.; Koshi, M. A novel route for PAH growth in HACA based mechanisms. *Combust. Flame* **2012**, *159* (12), 3589−3596.

(36) Chen, X.; Wang, X.; Fang, D. A review on C1s XPS-spectra for some kinds of carbon materials. *Fullerenes, Nanotubes Carbon Nanostruct.* **2020**, *28* (12), 1048−1058.

(37) Nakao, A.; Iwaki, M.; Sakairi, H.; Terasima, K. XPS characterization of nitrogen implanted silicon carbide. *Nucl. Instrum. Methods Phys. Res., Sect. B* **1992**, *65* (1-4), 352−356.

(38) Jansen, R. J. J.; van Bekkum, H. XPS of nitrogen-containing functional groups on activated carbon. *Carbon* **1995**, *33* (8), 1021−1027.